Kelvin–Helmholtz Instability "Tube" and "Knot" Dynamics. Part III: Extension of Elevated Turbulence and Energy Dissipation into Increasingly Viscous Flows

DAVID C. FRITTS,[a,b] LING WANG,[a] TOM LUND,[a] AND MARVIN A. GELLER[c]

[a] *GATS, Boulder, Colorado*
[b] *Embry-Riddle Aeronautical University, Daytona Beach, Florida*
[c] *Stony Brook University, State University of New York, Stony Brook, New York*

(Manuscript received 4 May 2023, in final form 29 February 2024, accepted 15 April 2024)

ABSTRACT: A companion paper by Fritts et al. reviews extensive evidence for Kelvin–Helmholtz instability (KHI) "tube" and "knot" (T&K) dynamics at multiple altitudes in the atmosphere and in the oceans that reveal these dynamics to be widespread. A second companion paper by Fritts and Wang reveals KHI T&K events at larger and smaller scales to arise on multiple highly stratified sheets in a direct numerical simulation (DNS) of idealized, multiscale gravity wave–fine structure interactions. These studies reveal the diverse environments in which KHI T&K dynamics arise and suggest their potentially ubiquitous occurrence throughout the atmosphere and oceans. This paper describes a DNS of multiple KHI evolutions in wide and narrow domains enabling and excluding T&K dynamics. These DNSs employ common initial conditions but are performed for decreasing Reynolds numbers (Re) to explore whether T&K dynamics enable enhanced KHI-induced turbulence where it would be weaker or not otherwise occur. The major results are that KHI T&K dynamics extend elevated turbulence intensities and energy dissipation rates ε to smaller Re. We expect these results to have important implications for improving parameterizations of KHI-induced turbulence in the atmosphere and oceans.

SIGNIFICANCE STATEMENT: Turbulence due to small-scale shear flows plays important roles in the structure and variability of the atmosphere and oceans extending to large spatial and temporal scales. New modeling reveals that enhanced turbulence accompanies Kelvin–Helmholtz instabilities (KHIs) that arise on unstable shear layers and exhibit what were initially described as "tubes" and "knots" (T&K) when they were first observed in early laboratory experiments. We perform new modeling to explore two further aspects of these dynamics: 1) can KHI T&K dynamics increase turbulence intensities compared to KHI without T&K dynamics for the same initial fields and 2) can KHI T&K dynamics enable elevated turbulence and energy dissipation extending to more viscous flows? We show here that the answer to both questions is yes.

KEYWORDS: Kelvin–Helmholtz instabilities; Mixing; Small-scale processes; Nonlinear models

1. Introduction

Observations of Kelvin–Helmholtz instabilities (KHIs) in the atmosphere, oceans, lakes, and the laboratory spanning over 70 years motivated a diversity of theoretical and modeling studies addressing secondary instabilities of KH billows driving turbulence transitions for various Richardson, Reynolds, and Prandtl numbers, Ri, Re, and Pr, spanning ~40 years. Of necessity, early three-dimensional (3D) theoretical and modeling efforts addressed instabilities of individual KH billows at very modest Re and Ri (Klaassen and Peltier 1985, 1991; Werne and Fritts 1999). Successive higher-resolution studies addressed increasingly smaller Ri and larger Re but continued to employ streamwise domains including one or several KH billows that were very narrow spanwise; see the reviews by Mashayek and Peltier (2012a,b) and Smyth and Moum (2012). Importantly, these domains specifically precluded descriptions of KHI "tube" and "knot" (T&K) dynamics first identified in laboratory shear-flow studies by Thorpe (1985, 1987; hereafter T85 and T87) seen to exhibit much more rapid turbulence transitions and suggested by Thorpe (2002) to be widespread in the atmosphere.

Only recently were a high-resolution, large-eddy simulation (LES) and several direct numerical simulations (DNSs) of KHI performed employing sufficiently wide domains and high resolution to enable the emergence of T&K dynamics and exploration of their evolutions. Those studies to date include the following:

1) Fritts et al. (2021; hereafter F21) performed a high-resolution compressible LES that accounted for multiple KHI T&K features observed at a high altitude in the atmosphere by Hecht et al. (2021; hereafter H21) and seen in the early laboratory studies (T85, T87).
2) Fritts et al. (2022a,b; hereafter F22a, F22b) described a DNS including two forms of KHI T&K dynamics and their implications for elevated energy dissipation rates ε; however, it employed a noise seed that did not enable several important forms of these dynamics.
3) Fritts et al. (2022c; hereafter F22c) used results of the F22a DNS to approximate observations of apparent KHI

Denotes content that is immediately available upon publication as open access.

Corresponding author: David C. Fritts, dave@gats-inc.com

DOI: 10.1175/JAS-D-23-0085.1

T&K features observed in polar mesospheric clouds (PMCs).

4) A companion paper by Fritts and Wang (2023; hereafter FW23) revealed multiple, local KHI T&K events in an idealized multiscale gravity wave–fine structure superposition.
5) Mixa et al. (2023; hereafter M23) performed a high-resolution compressible LES designed to approximate observed KHI dynamics in the lower thermosphere and assess the resulting mixing.

The potential dynamical importance of KHI in the atmosphere and oceans derives from their expected contributions to turbulence and mixing. These roles are widely acknowledged in the oceans, where mixing due to small-scale KHI is expected to be an important, and potentially the dominant, contributor to small-scale mixing accompanying the ocean internal gravity wave (GW) spectrum that drives the ocean meridional overturning circulation (Gregg et al. 2018; Mashayek et al. 2015).

KHIs are also an important component of parameterization efforts addressing mixing in the atmospheric stable boundary layer, e.g., Fernando and Weil (2010). But their potential to contribute significant turbulence, mixing, and transport appears to be much less appreciated in the atmosphere at higher altitudes. This is true in the stratosphere, where observations provide few constraints at small vertical scales and model resolutions are often much coarser than expected KHI events that can extend to very small scales at large Re. It is also true in the mesosphere and lower thermosphere (MLT), where KHI T&K dynamics are prolific (Fritts et al. 2023, hereafter F23; H21), but very few observations can resolve fine structure scales enabling KHI. Additionally, current mixing parameterizations based only on assumed GW breaking appear to be insufficient to account for observed mean constituent profiles in the MLT (Garcia et al. 2014; Liu 2019).

Given the above, our objectives in this paper are as follows:

1) Employing a high-resolution DNS to explore and quantify new KHI T&K dynamics not seen to arise in the many idealized KHI studies to date, nor in the initial KHI T&K DNS described by F22a,b
2) Employing a high-resolution DNS for the same initial conditions in a narrow spanwise domain excluding T&K dynamics to enable the evaluation of T&K ε enhancements
3) Employing DNS of the two cases for decreasing Re in order to (i) assess the impacts on T&K dynamics and energetics and (ii) explore to what degree KHI T&K dynamics enable turbulence transitions at Re for which they would not otherwise occur
4) Comparing and contrasting the KHI T&K DNS described by F22a,b and the similar case presented here to reveal the broader range of KHI T&K dynamics and the influences of a later noise seed approximating the influences of persistent small-scale turbulence

The model employed for this study is described in section 2. DNS of KHI with and without T&K dynamics for Re = 5000 and for decreasing Re are described in sections 3 and 4. Section 5 compares the turbulence transitions in narrow and wide domains and their implications for energy dissipation rates with decreasing Re. Energy dissipation rate probability density functions (PDFs) and spectra for the varying Re are described in section 6. A discussion of these results relative to previous studies and their implications for parameterizations of KHI T&K dynamics are provided in section 7. Our conclusions are presented in section 8.

2. Model description, domain, initial conditions, and visualization methods

a. Model description

Following F22a, we employ the spectral atmosphere model (SAM), a Fourier, pseudospectral, triply periodic model that solves the Boussinesq Navier–Stokes equations written as

$$\frac{\partial u_j}{\partial x_j} = 0, \tag{1}$$

$$\frac{\partial u_i}{\partial t} + \frac{\partial u_i u_j}{\partial x_j} + \frac{1}{\rho_0}\frac{\partial p'}{\partial x_i} = \frac{\theta'}{\theta_0} g\delta_{i3} + \nu\frac{\partial^2 u_i}{\partial x_j \partial x_j}, \tag{2}$$

$$\frac{\partial \theta}{\partial t} + \frac{\partial \theta u_j}{\partial x_j} = \kappa\frac{\partial^2 \theta}{\partial x_j \partial x_j}. \tag{3}$$

Here, $u_i = (u_1, u_2, u_3)$ are the velocity components along x, y, and z; p, ρ, and θ are the pressure, density, and potential temperature (with $\theta = T$ for a Boussinesq flow), respectively; and ν and κ are the kinematic viscosity and thermal conductivity, respectively. Additionally, primes and "0" subscripts denote perturbation and mean quantities, respectively, and successive indices imply summation (see Table 1 for symbols and abbreviations).

SAM is highly optimized for massively parallel computing. It employs a pseudospectral algorithm to compute nonlinear products and removal of aliasing errors using the two-third truncation rule (Patterson and Orszag 1971). SAM uses a low-storage, third-order Runge–Kutta method for time advancement, accuracy, and efficiency (see F22a for additional details). SAM also now employs a "pencil" domain decomposition that allows the computational load to be distributed over many more processors.

In this application, we employ SAM for 1) DNS of multiple, interacting KH billows in a wide domain allowing varying KHI phases ϕ and wavelengths λ_h and T&K dynamics along their axes and 2) corresponding DNS in a narrow domain that precludes T&K dynamics. The initial noise seed was chosen to enable the emergence of KHI that are initially misaligned and discontinuous along y at finite amplitudes, hence features not described by F22a. A single DNS for Re = 5000 having a spatial resolution of $(N_x, N_y, N_z) = (432, 1296, 432)$ sufficient to describe the initial, large-scale, responses for all Re was initialized with a white noise seed and extended to $0.38T_b$ (with T_b being the buoyancy period at the peak stability) at $z = 0$ and $t = 0$ at which time weak, but coherent, KH billows arose. The same procedure was employed for DNS in a small domain. These fields were employed to continue the DNS for Re = 5000, 3000, 2000, 1000, and 500 in order to assess the impacts of decreasing Re on the KHI T&K evolutions and

TABLE 1. Symbols and abbreviations.

ε	Energy dissipation rate	F16	Fritts et al. (2016)
$\overline{\varepsilon}$	Mean ε	F21	Fritts et al. (2021)
λ_h	KHI wavelength	F22a,b,c	Fritts et al. (2022a,b,c)
λ_x	KHI wavelength along x	F23	Fritts et al. (2023)
ϕ	KH billow phase along y	FW23	Fritts and Wang (2023)
L	A reference KHI λ_x; $L = X/3$	H21	Hecht et al. (2021)
Pr	Prandtl number	(I)GW	(Inertia) gravity wave
Re	Reynolds number	KHI	Kelvin–Helmholtz instability
Ri	Richardson number	LES	Large eddy simulation
T_b	Buoyancy period	M23	Mixa et al. (2023)
x, y, z	Domain axes	MLT	Mesosphere and lower thermosphere
X, Y, Z	Domain dimensions	PDF	Probability density function
3D	Three-dimensional	SAM	Spectral atmosphere model
CI	Convective instabilities	T&K	"Tube" and "knot"
DNS	Direct numerical simulation	T85, T87	Thorpe (1985, 1987)

turbulence intensities, their implications for enhanced turbulence, and the potential for turbulence and mixing where it might not occur without T&K dynamics. A maximum of 3600 cores were employed for the KHI T&K Re = 5000 DNS. The smaller Re required smaller computational resources, i.e., 2700, 1920, 1440, and 960 cores, respectively.

b. Initial conditions and domain specification

As in F22b, we specify a shear flow approximating a steepened inertia–GW (IGW) having localized shear and stability maxima, with the mean wind and stability profiles given by

$$U(z) = U_0 \cos\left(\frac{\pi z}{Z}\right) \tanh\left(\frac{z}{h}\right), \tag{4}$$

$$N^2(z) = N_0^2 + (N_m^2 - N_0^2)\,\mathrm{sech}^2\left(\frac{z}{h}\right), \tag{5}$$

where Z is the domain depth, $z = 0$ at the domain center, U_0 is the half-shear velocity difference, h is the half-shear depth, and we assume $N_0^2 = (g/\theta)d\theta/dz = 10^{-4}\ \mathrm{s}^{-2}$ external to the shear layer and $N_m^2 = 8N_0^2$, because large shear and stability enhancements arise in thin layers due to GW interactions in multiscale environments (Fritts et al. 2016, hereafter F16; FW23). The choice for N_m yields a maximum buoyancy period $T_b = 2\pi/N_m = 222$ s.

The remaining parameters include a minimum Richardson number, $\mathrm{Ri} = N_m^2/(dU/dz)^2 = 0.1$, a maximum Reynolds number, $\mathrm{Re} = U_0 h/\nu = 5000$, and a Prandtl number, $\mathrm{Pr} = \nu/\kappa = 1$, to impose the same resolution requirements for the velocity and temperature fields. Re = 5000 is appropriate for a KHI $\lambda_h \sim 100$ m, a shear depth $h \sim 0.07\,\lambda_h$, and $\nu \sim 0.15\ \mathrm{m}^2\ \mathrm{s}^{-1}$ at an altitude of ~60 km. In reality, KHI λ_h can exceed ~300 m in the SBL (Blumen et al. 2001), ~5 km in the troposphere and stratosphere (Luce et al. 2007, 2018), and ~5–15 km in the MLT (H21; F23), implying a true Re (assuming no background turbulent viscosity) that can be orders of magnitude larger at all altitudes below ~80–100 km. Importantly, however, Re = 5000 requires very computationally intensive DNS but enables secondary KHI to compete with secondary convective instabilities (CIs) and T&K dynamics where they arise, thus ensuring a reasonable assessment of enhanced turbulence and mixing accompanying KHI T&K dynamics.

To ensure validity of SAM in these applications, we assume an approximate KHI wavelength $\lambda_h \sim L$ for fixed length scale $L = 2$ km, with wavenumber $k_h = 2\pi/\lambda_h$, a shear half-depth $h = 0.07$, $L = 140$ m, and $U_0 = 12.5\ \mathrm{m\ s}^{-1}$. We also specify an elevated "turbulence" viscosity, $\nu = \nu_{\mathrm{turb}} = 0.35\ \mathrm{m}^2\ \mathrm{s}^{-1}$, to approximate turbulence influences in the middle/upper stratosphere because small-scale turbulence is expected to be pervasive and turbulence ε decays slowly over multiple T_b (F16, F22c). The initial fields are illustrated in Fig. 1 for a periodic domain of depth $Z = 3L$ and periodic U, $d\theta/dz$, and N^2, enabling a pseudospectral SAM DNS. Horizontal domain dimensions along the shear and the nominal KH billows are $X = 3L$ and $Y = 9L$. The choice for h assumed above is somewhat smaller than the linear stability KH λ_h estimate to enable primarily 3, but occasionally 4, initial KH billows to arise along the X domain. The large $Y = 9L$ enables significant KH billow phase variations and misalignments along y; the $Z = 3L$ domain depth enables strong T&K dynamics extending well away from the initial shear.

c. Noise seed and DNS compliance

The nondivergent white noise seed noted above with $u_{\mathrm{rms}} = 10^{-3}U_0$ yields perturbations that initiate KH billows having 1) three or four initial KHI λ_h along x at different y yielding several regions along y of misaligned KH billows not described by F22a, 2) smaller-scale secondary CI in the billow cores, 3) intermediate-scale T&K dynamics as variable billow core phases arise, and 4) secondary KHI in the stratified braids where they are distorted by larger-scale T&K dynamics.

Importantly, the noise seed was chosen specifically to include T&K dynamics not addressed by F22a. The specified Re = 5000 enables the performance of a multibillow DNS and a motion spectrum having an extensive turbulence inertial range that together span over 3 decades of scales. We note that our specified Re is appropriate for KHI $\lambda_h \sim 2$–5 km at higher altitudes, but it is significantly smaller than appropriate with weak or no initial turbulence viscosity for larger KHI $\lambda_h \sim 0.5$–5 km seen at lower altitudes, as noted above.

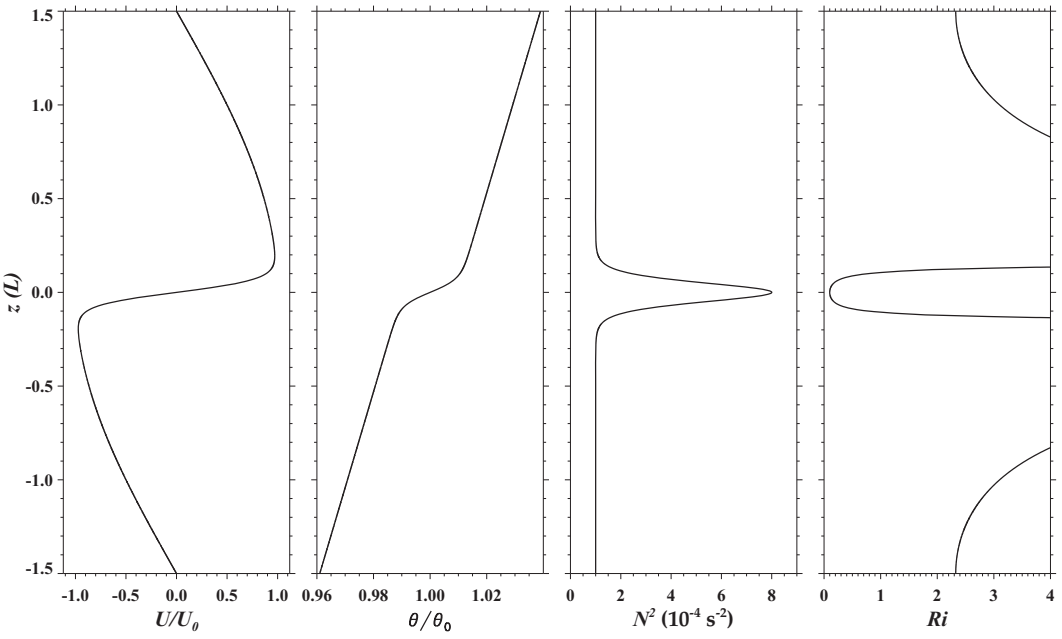

FIG. 1. Initial vertical profiles of U/U_0, θ/θ_0, N^2, and Ri employed for our DNS.

A DNS imposes significant resolution and computational resource requirements to describe turbulence approaching the Kolmogorov scale,

$$\eta = (\nu^3/\overline{\varepsilon})^{1/4}, \tag{6}$$

for the mean energy dissipation rate,

$$\overline{\varepsilon} = 2\nu\langle S_{ij}S_{ij}\rangle, \tag{7}$$

where angle brackets denote spatial averaging, and strain tensor components are defined as

$$S_{ij} = \frac{1}{2}\left(\frac{\partial u_i}{\partial x_j} + \frac{\partial u_j}{\partial x_i}\right). \tag{8}$$

To achieve true DNS, we employ isotropic resolution and ensure that

$$\Delta x < 1.8\eta \tag{9}$$

is satisfied throughout the evolution (Moin and Mahesh 1998; Pope 2000).

Importantly, the above constraint assumes isotropic homogeneous turbulence, which does not account for initial instabilities and very localized, small-scale turbulence generation. Thus, we define a more realistic (and more computationally costly) required resolution by assessing local $\overline{\varepsilon}$ on all 2D planes normal to x, y, and z and use the smallest obtained $\overline{\eta}$ (typically on the x–y plane at $z = 0$). This implies a highest required resolution of $(N_x, N_y, N_z) = (3600, 10\,800, 3600)$ employing (2400, 7200, 2400) spectral modes with the "two-thirds" rule spectral truncation (Patterson and Orszag 1971) to eliminate aliasing errors. The simulation is run using N_z cores for each stage of the remeshing sequence, requiring a maximum of 3600 cores at the most intense phase, and a CFL of 0.9 assures numerical stability. Given the required de-aliasing scheme, the smallest length scale (Fourier mode wavelength) that is resolved in each direction is $3\Delta x$. At the stage of most intense turbulence, this corresponds to a minimum resolved spatial scale of $0.000\,833X$ and 1200 resolved modes along x.

d. *Three-dimensional visualization*

The 3D imaging of the vorticity dynamics underlying the KHI T&K evolutions described here employs the same methods used by FW23. The negative second eigenvalue λ_2 of the tensor $L = R^2 + S^2$ corresponds to features having strong rotation, as opposed to shearing, and its magnitude measures rotational intensity (Jeong and Hussain 1995). Components of the strain tensor S are given in Eq. (8); those for the rotation tensor are

$$R_{ij} = \frac{1}{2}\left(\frac{\partial u_i}{\partial x_j} + \frac{\partial u_j}{\partial x_i}\right). \tag{10}$$

Thus, negative λ_2 reveals the features of the vorticity field accounting for turbulence dynamics driving the majority of the turbulence cascade. This allows tracking the transition from initial vortex sheets to emerging vortex tubes, their interactions in knot regions exciting Kelvin (1880) vortex waves, or "twist waves" (Arendt et al. 1997; Fritts et al. 1998), their fragmentation of the parent vortices, and similar interactions driving inertial-range turbulence, as employed by FW23 and other applications noted therein. In contrast, the 2D imaging of ε on individual x–y and x–z planes is employed to reveal the relative contributions of the various

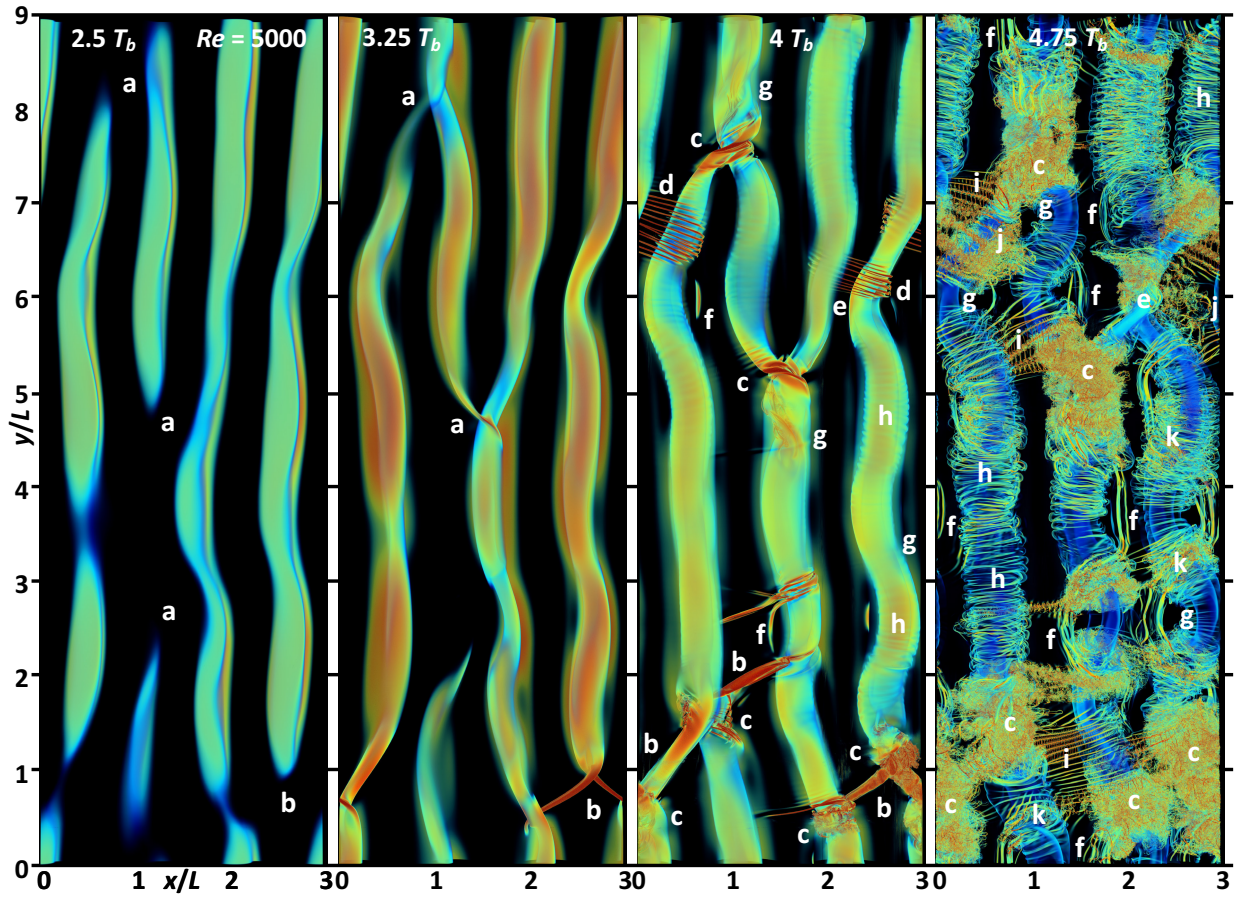

FIG. 2. The 3D imaging of λ_2 at $z = 0$ viewed from above at 2.5, 3.25, 4, and 4.75T_b for Re = 5000. The value λ_2 varying from black to red shows increasing rotation. Labels a–k denote feature described in the text. Large-scale vorticity is along y. The λ_2 color scales extend from near zero to maxima that increase by factors of 100, 140, and 4 at successive times. The major responses occur in a depth of 0.4L centered at $z = 0$.

T&K dynamics to the overall event energy dissipation in each case. The difference in this imaging is because the ε fields emphasize the smallest spatial scales; hence, they do not as readily reveal the underlying turbulence transitions and dynamics.

3. KHI T&K dynamics and energy dissipation rates for Re = 5000

a. *KHI T&K dynamics in a wide domain*

A SAM DNS enabling KHI T&K dynamics for Re = 5000 is shown with 3D λ_2 fields viewed from above from 2.5 to 4.75T_b after the initial noise seed in Fig. 2. The interval extends from the emergence of initial KH billows to T&K dynamics driving secondary instabilities and initial turbulence transitions. The initial noise seed here enables an expanded range of T&K features relative to the initial DNS study by F22a. The absence of a second noise seed at the onset of turbulence transitions in this case precludes other T&K features described by F22a. Note that the times employed here are ~0.75T_b later than in F22a at the same evolution stages. Features common to F22a and the DNS described here seen in the full domain in Fig. 2 and the expanded views in Fig. 3 include the following:

1) Weak initial KH billows exhibit varying λ_h and phases along y (sites "a")
2) Large-scale vortex tubes arise on the vortex sheets between KH billows where they exhibit significant phase variations along y, e.g., large $|d\phi/dy|$ (sites "b")
3) Vortex tubes that intensify, wrap under and over adjacent KHI billows at smaller and larger x, and "attach" to the billows inducing the formation of vortex "knots" that account for rapid transitions to strong turbulence thereafter (sites "c" at smaller y)
4) Large-scale billow core twist waves induced by the vortex knots (sites "g")
5) Secondary KHI and CI that drive slower and weaker turbulence transitions thereafter (sites "f" and "h")
6) Secondary T&K dynamics on intensifying vortex sheets between adjacent billows (sites "i" at 4.75T_b)
7) Smaller-scale twist waves arising due to roughly orthogonal interactions among adjacent vortices in close proximity (sites "j")

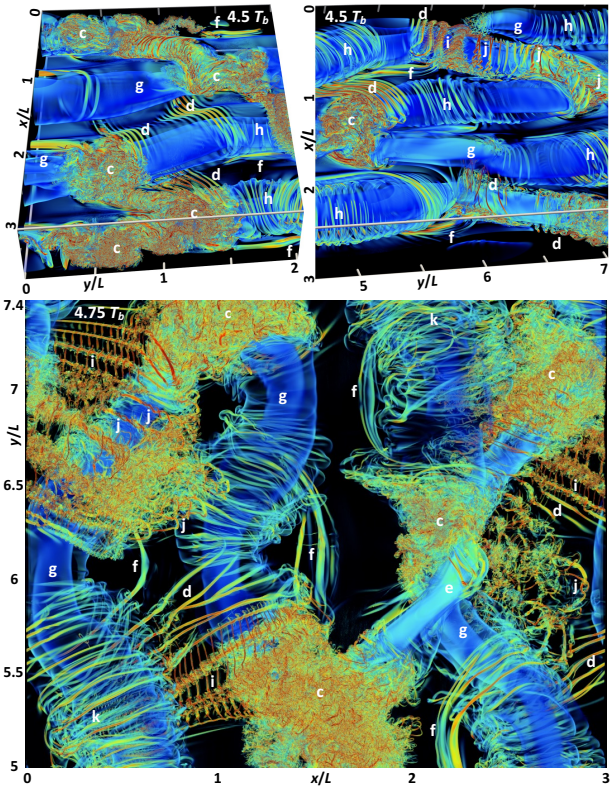

FIG. 3. Subdomain views of the λ_2 field shown at (top) $4.5T_b$ in Fig. 2 at smaller and larger y/L viewed from larger x and z and (bottom) upper-right panel at $4.75T_b$ in Fig. 2 viewed from above. Feature labels are described in the text. The smallest resolved features have scales $\sim L/300$.

8) Interactions of the secondary CI and KHI where they are advected into close proximity wrapping around the KH billows (sites "k")

Features arising in the DNS described here not seen by F22a include the following:

9) Intense KH billow interactions arising where 1 billow "end" emerges adjacent to 2 where they are misaligned along y (sites "c" at larger y at $4T_b$)
10) A localized KH billow pairing event also inducing a vortex knot (site "e")

Also seen emerging by $2.5T_b$ and intensifying strongly thereafter are KH billow displacements along x that are coherent among adjacent billows at larger x extending from $y/L \sim 1$–6. These are a manifestation of an additional axial KHI instability referred to as a "bending" instability (Rogers and Moser 1992; Kit et al. 2010), which we denote as "crankshaft" instabilities, given their varying axial forms that arise for the range of Re explored here. The vortex dynamics accounting for these crankshaft instabilities are the self-advection of the KH billows where they exhibit a curvature that induces vertical motions as seen for vortex rings. Upward (downward) vertical advection leads to advection toward positive (negative) x in the mean shear flow having

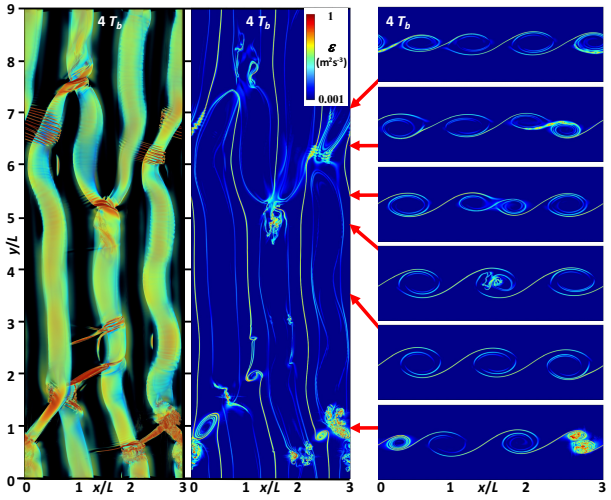

FIG. 4. (left) The 3D imaging of $\lambda_2(x, y)$ as in Fig. 2 at $4T_b$ and the corresponding 2D cross sections of $\log_{10}\varepsilon(x, y)$ at (center) $z = 0$ and (right) y indicated by the red arrows for the wide-domain Re = 5000 simulation. The color scale for ε is shown at the center top.

$dU/dz > 0$, yielding intensifying curvature of the KH billows in time.

b. KHI T&K energy dissipation rates in a wide domain

Cross sections of $\log_{10}\varepsilon(x, y)$ at $z = 0$ and $\log_{10}\varepsilon(x, z)$ at representative y for the wide domain Re = 5000 simulation are shown with reference to the corresponding $\lambda_2(x, y)$ fields at 4, 4.75, and $5.5T_b$ in Figs. 4–6. Cross sections, rather than volumetric imaging, are used for $\log_{10}\varepsilon$ to reveal the dynamics accounting for these various responses because volumetric views mask the responses at $z = 0$. The $\log_{10}\varepsilon(x, z)$ cross sections at $4T_b$ in Fig. 4 reveal emerging enhancements of ε accompanying initial T&K interactions of adjacent billow cores at different y that drive the initial twist wave generation and cascades to smaller scales (as initially described by F22a,b for a different initial noise seed). Three of these at top right reveal

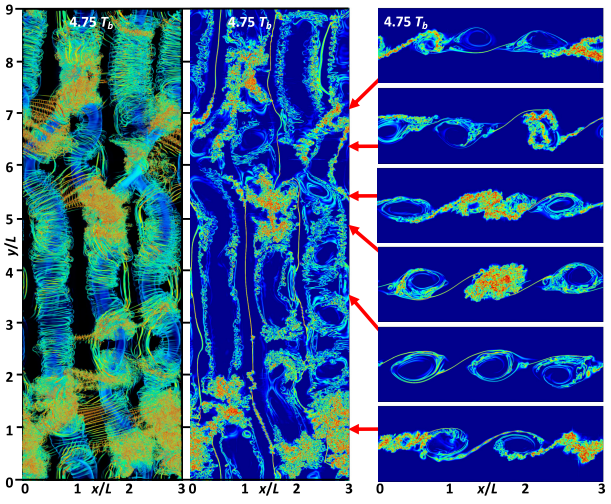

FIG. 5. As in Fig. 4, but at $4.75T_b$.

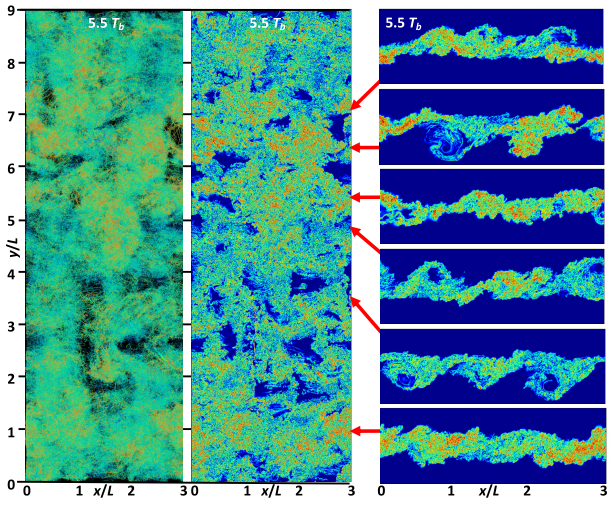

FIG. 6. As in Figs. 4 and 5, but at $5.5T_b$.

emerging strong interactions where four initial KH billows link to three at larger or smaller y and have become strongly kinked along y by $4T_b$ (see these regions from $y/L \sim 4$–9 in Figs. 2 and 3). The fourth and fifth $\log_{10}\varepsilon(x, z)$ cross sections at right reveal only three KH billows that are relatively uniform. A sixth $\log_{10}\varepsilon(x, z)$ cross section at bottom right in Fig. 4 shows two vortex tubes in cross section at right that have evolved on the intensified vortex sheets linking three KH billows where they exhibit significant initial phase variability.

Cross sections of these fields at 4.75 and $5.5T_b$ in Figs. 5 and 6 reveal significant further evolutions of the KHI T&K dynamics in the five significantly disturbed regions (and the exception) highlighted at right in Fig. 4. Specific features of relevance include the following:

1) Adjacent billows merge and entwine by $4T_b$ (see Fig. 4 at left) where they are initially misaligned along y and yield intense vortex knots, local turbulence, and ε by $4.75T_b$; see especially these regions at $y/L \sim 5$–6 and 7–8, and $x/L \sim 1$–2 in Fig. 5.
2) Other knots arise where billow cores exhibit significant $d\phi/dy$; these sites further intensify the intermediate vortex sheets due to additional stretching along y that induces larger- and smaller-scale vortex tubes by $4T_b$ (see Figs. 2 and 4 and F22a).
3) Local T&K site turbulence at $4.75T_b$ spreads dramatically along the vortex tubes and throughout the billow cores by $5.5T_b$, but initially less impacted billow cores remain partially laminar.
4) The initial shear layer becomes largely turbulent by $5.5T_b$, and $\overline{\varepsilon}$ achieves its maximum at $\sim 6.2T_b$ (see the solid red line at left in Fig. 7).

c. *KHI T&K dynamics and energy dissipation rates in a narrow domain*

To assess the enhancement of local ε in the simulation enabling KHI T&K dynamics, we performed a narrow-domain simulation having $Y/L = 1$ to exclude T&K dynamics employing a noise seed of equal amplitude. The results are shown with $\log_{10}\varepsilon$ cross sections from 4.25 to $5T_b$ in Fig. 8 in the same formats as in Figs. 4–6. In this case, no significant interactions among adjacent KH billows occur and only secondary CI arises and drives turbulence transitions thereafter, despite extending to later times than shown for the KHI T&K dynamics discussed above. The temporal evolution of $\overline{\varepsilon}$ in this case is shown with a dashed red line in Fig. 7 at left, and it achieves ~95% of its initial maximum value at $5T_b$. Specific additional features include the following:

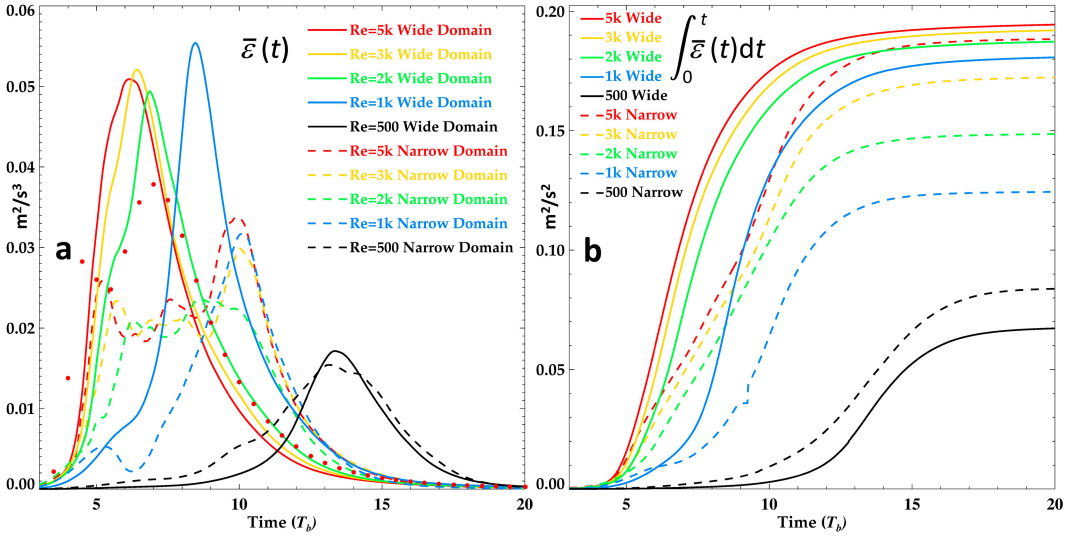

FIG. 7. (a) Temporal and (b) cumulative evolutions of $\overline{\varepsilon}$ averaged over the full (x, y) domain and a depth of $0.4L$ centered at $z = 0$ for the wide and narrow domains (solid and dashed lines) for Re = 5000 and the smaller Re. Color codes are shown in each panel. Red dots show the corresponding $\overline{\varepsilon}$ temporal evolution at $0.5T_b$ intervals for the F22a,b DNS.

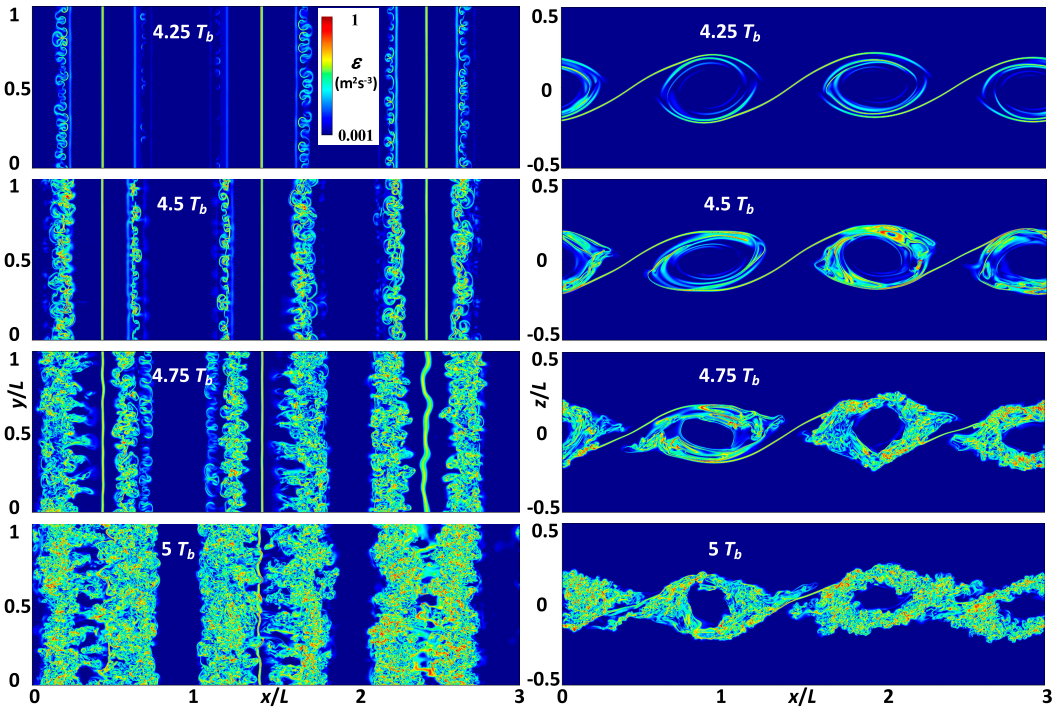

FIG. 8. The 2D $\log_{10}\varepsilon(x, y)$ cross sections at $z = 0$ and (x, z) at $y/L = 0$ for the narrow-domain Re = 5000 simulation. The color scale is as in Figs. 4–6.

1) The only contributions to ε prior to $4.5T_b$ are in the laminar vortex sheets between KH billows and the emerging CI having spanwise scales $\sim 0.1L$ in the outer billow cores.
2) Intensifying CI expands and begins to interact with the vortex sheets by $\sim 4.5T_b$.
3) These dynamics expand into the billow cores thereafter (see Fig. 8) and yield an initial peak $\overline{\varepsilon}$ at $\sim 5.2T_b$ (see Fig. 7).
4) Successive, variable peak $\overline{\varepsilon}$ occur at ~ 7.5 and $10T_b$ thereafter (see Fig. 7 at left).
5) Cumulative $\overline{\varepsilon}$ (red dashed line at right in Fig. 7) is surprisingly only ~3% less than for the wide domain because peak $\overline{\varepsilon}$ is smaller, but large $\overline{\varepsilon}$ spans a longer interval.

4. KHI T&K dynamics for decreasing Re

We now explore the influences of decreasing Re on KHI evolutions, the T&K dynamics that arise, and their implications for turbulence transitions and intensities. All cases employ the same initial noise seed to ensure that the initial KH billows have common features along y. Evolutions of the vorticity fields for Re = 3000, 2000, 1000, and 500 are compared with that for Re = 5000 over intervals extending to later times for decreasing Re due to increasing viscous influences. Temporal and cumulative $\overline{\varepsilon}$ evolutions for the wide and narrow domains are shown in Fig. 7; ε probability density functions and spectra are compared in section 6.

a. *KHI T&K dynamics at Re = 3000*

The evolution for Re = 3000 shown at top in Fig. 9 not only closely parallels that for Re = 5000 but also exhibits delayed and/or weaker responses at most sites. The λ_2 color scale varies in time to reveal the key features at each. Initial larger-scale billow interactions are nearly identical to those at Re = 5000 because the increase in viscosity has weak influences on the KH billow scales and initial links and hence only weakly impacts turbulence transitions and scales arising in the initial knots. However, they significantly impact the emergence of secondary KHI, CI, larger- and smaller-scale vortex tubes, and their initial turbulence transitions in the absence of T&K enhancements, causing these responses to be much weaker than seen for Re = 5000 in Fig. 2.

Significant differences in the Re = 3000 evolution relative to Re = 5000 include 1) delayed knot formation due to weaker and fewer adjacent billow attachments, 2) slower initiation of larger-scale twist waves, 3) weaker, delayed, and less extended vortex tubes, 4) significantly delayed emergence and evolutions of secondary KHI, CI, and their interactions, and 5) fewer and delayed turbulence transitions, especially accompanying smaller-scale vortex tubes; compare sites labeled "a–d" and "f–k" for the two Re.

The crankshaft instability emerging at $4T_b$ and becoming prominent by $4.75T_b$ at smaller y for Re = 5000 is seen much more clearly for Re = 3000 due to the weaker secondary CI at $4.75T_b$ (see sites "l"). The instability wavelength is comparable to that estimated for Re = 5000 at $4.75T_b$, i.e., $\lambda_y \sim 2.25L$. This instability also plays a clear role in the occurrence of secondary KHI that will be seen below to become more prominent at smaller Re.

Differing KHI interaction dynamics and secondary instabilities occurring for Re = 3000 are seen in Fig. 7 to delay but

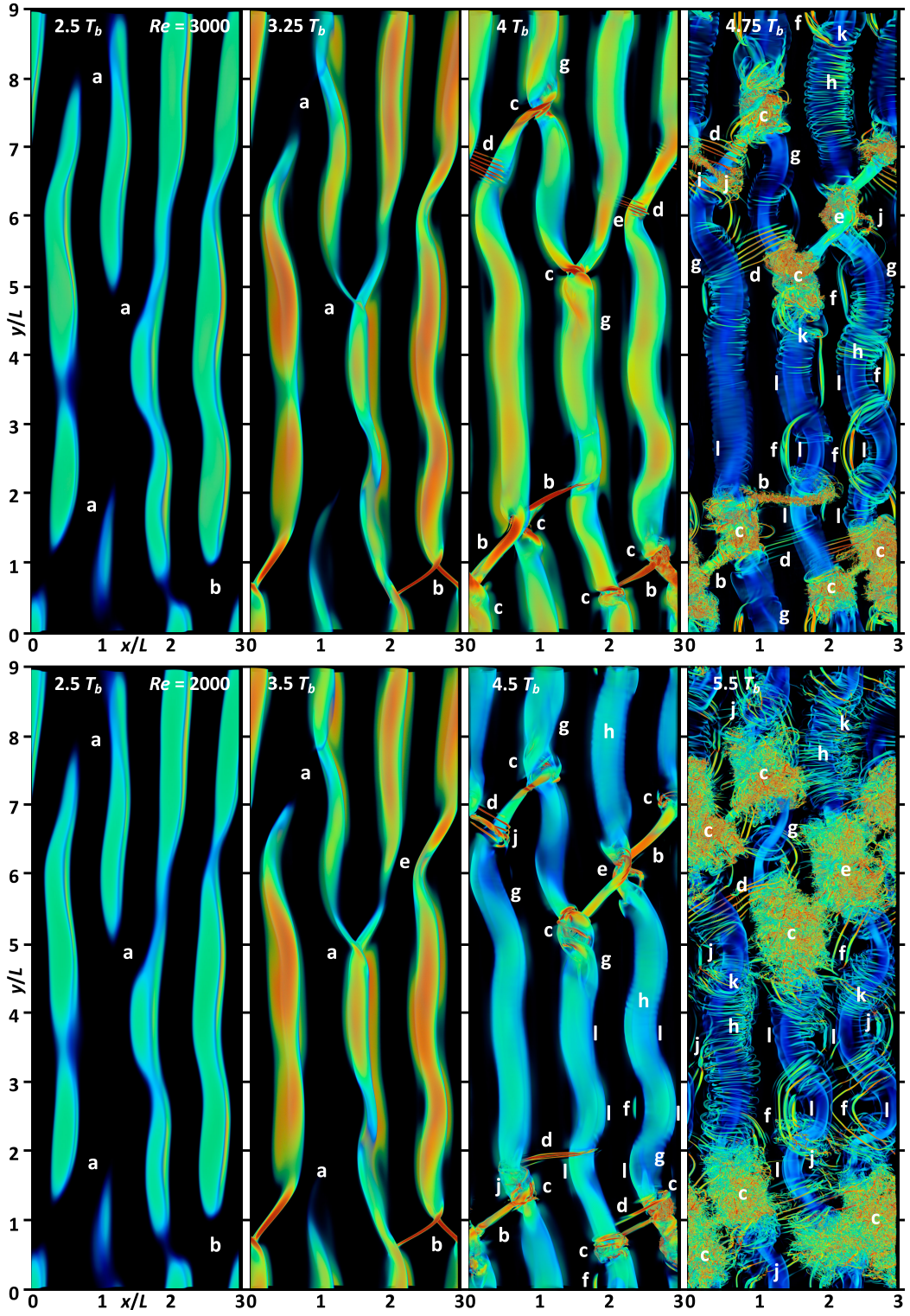

FIG. 9. The 3D imaging of $\lambda_2(x, y)$ as in Fig. 2 at (top) 2.5, 3.25, 4, and $4.75T_b$ for Re = 3000 and (bottom) 2.5, 3.5, 4.5, and $5.5T_b$ for Re = 2000. Labels "a"–"l" are as in Figs. 2 and 3 and denote feature evolutions at both Re values described in the text.

enable, a higher, more transient, peak $\overline{\varepsilon}$, and a cumulative $\overline{\varepsilon}$ only ~1% smaller than occurs for Re = 5000.

b. KHI T&K dynamics at Re = 2000

The Re = 2000 evolution shown at the bottom in Fig. 9 exhibits multiple features that parallel those seen for Re = 5000 and 3000 but evolve more slowly. Links among adjacent billows arise somewhat later for Re = 2000 and exhibit weaker responses but largely retain the same T&K features and knot locations, the latter of which are more widespread at the last time shown.

The crankshaft instability emerging by $4.75T_b$ for larger Re intensifies strongly from 3.5 to $5.5T_b$ for Re = 2000 despite the slower evolutions of the underlying KHI. Its wavelength is the same as for the larger Re at $4.75T_b$, $\lambda_y \sim 2.25L$, as constrained by the periodic y domain. It also exhibits a weak third harmonic yielding an emerging, roughly square-waveform at Re = 2000 at smaller y by $5.5T_b$ and extends a comparable distance along y as at larger Re by $4.75T_b$.

These varying Re = 2000 KHI and secondary instability dynamics are seen in Fig. 7 to yield a slightly delayed (~0.5–$0.7T_b$) and slightly smaller (~3%–5%) peak $\overline{\varepsilon}$ and a cumulative $\overline{\varepsilon}$ only ~4% smaller than occur for Re = 5000.

c. KHI T&K dynamics at Re = 1000

The Re = 1000 evolution shown at the top in Fig. 10 exhibits significant departures from those at higher Re despite sharing the initial noise seed. As discussed above, all higher Re fields reveal links between adjacent billows at small amplitudes leading to sites where 1) one billow links to two where their initial "ends" are misaligned and 2) adjacent billows link via larger- and/or smaller-scale vortex tubes emerging in regions of significant phase variability along y.

In contrast, the Re = 1000 evolution reveals links among the misaligned initial responses yielding continuous adjacent billows exhibiting similar phase variability along y that link via small-scale vortex tubes thereafter (cf. sites "a–c" for Re = 1000 in Fig. 10 with those for the larger Re). These lead to limited bands at $y/L \sim 1$ and 6 in which small-scale vortex tubes between adjacent billows lead to relatively weak knots at $6.5T_b$ (sites "c") in which the weak initial turbulence is largely confined.

Also seen are crankshaft instabilities emerging by $4.5T_b$ that exhibit strong, roughly square-wave responses by $6.5T_b$ (sites "l"). The strong billow distortions induce additional, smaller-scale vortex tubes where adjacent KH billows are closely spaced (sites "d"), secondary KHI where billow curvature is strong (sites "f"), and large-scale twist waves in the distorted billow cores (sites "g"). These vortex dynamics and associated turbulence are delayed relative to those arising for Re = 2000 and larger. Importantly, however, the turbulent knots seen at $6.5T_b$ have already yielded a broad turbulence spectrum and are almost certainly unable to account for the peak $\overline{\varepsilon}$ for this case, which is ~6 times larger and occurs ~$2T_b$ later. The only remaining potential sources of stronger turbulence at later times are the intensified and highly distorted KH billows (see the discussion in section 5 and Fig. 12).

d. KHI T&K dynamics at Re = 500

The Re = 500 evolution shown in the lower panels in Fig. 10 also departs significantly from those at larger Re employing the same initial noise seed. Unlike the evolutions for larger Re, it exhibits neither misaligned KH billows nor T&K dynamics until after $11T_b$. This more viscous shear flow evolves very slowly and induces pairing of weak initial billows that result in only 2 KH billows at finite amplitudes along x (sites "m") by $9T_b$. The initial noise seed and the interactions among adjacent billows as they merge induce crankshaft responses in the regions of initial billow pairing that are coherent along x and have the same wavelength seen to emerge at larger Re at later times (sites "l"). In this case, however, the third harmonic is reversed in phase and results in an intensifying "sawtooth" form at later times.

The maxima of these responses displaced toward positive x (sites "n") occur above the initial shear layer center and exhibit highly distorted secondary KHI at their maximum upward displacements. Vortex tubes (sites "o") emerge only after $11T_b$, implying no role for T&K dynamics in turbulence transitions in (sites "p") accounting for the peak $\overline{\varepsilon}$ thereafter.

5. Comparisons of turbulence transitions in wide and narrow domains

Figure 7 at left reveals that turbulence transitions driving $\overline{\varepsilon}$ increases are slower for Re decreasing from 5000 to 500 in both wide and narrow domains. T&K dynamics are less constrained by decreasing Re because they arise at the KH billow scales. Secondary KHIs are not expected for the specified Ri and Re but are enabled where billow curvature intensifies the vortex sheets between adjacent billows for all Re examined here. Secondary CIs, in contrast, are expected but arise at spatial scales that increase significantly with decreasing Re.

Figure 11 shows narrow domain responses for Re decreasing from top to bottom at the last times shown for these cases in Figs. 2, 9, and 10. These include 3D imaging of $\lambda_2(x, y)$ in a volume of depth $\Delta z = 0.4L$ centered at $z = 0$ (left) and $\log_{10}\varepsilon(x, y)$ and (x, z) cross sections at $z = 0$ and $y = 0$ at center and right, respectively. Whereas Fig. 2 for Re = 5000 reveals widespread secondary CI where the billows do not exhibit a strong curvature (see the relatively uniform billow at $x/L \sim 2$ and $y/L \sim 8$), those seen for decreasing Re in Figs. 9 and 10 reveal strongly suppressed or absent secondary CI compared to the narrow domain fields in Fig. 11. Thus, the expectations that secondary CIs are the major driver of turbulence for uniform KH billows at smaller Re, and that secondary KHIs only contribute for larger Re, are the opposite of what occurs in KHI T&K environments if the wide-domain results described here are representative. Importantly, both play much less significant roles than the larger-scale T&K dynamics.

Corresponding $\log_{10}\varepsilon(x, y)$ cross sections at $z = 0$ for the wide-domain KHI T&K dynamics for decreasing Re at 4.75, 5, 5.5, 7.5, and $12T_b$ are shown from left to right in Fig. 12. These times are slightly later for Re = 3000 and 1000 in order to show all fields when the large domain $\overline{\varepsilon}$ is increasing

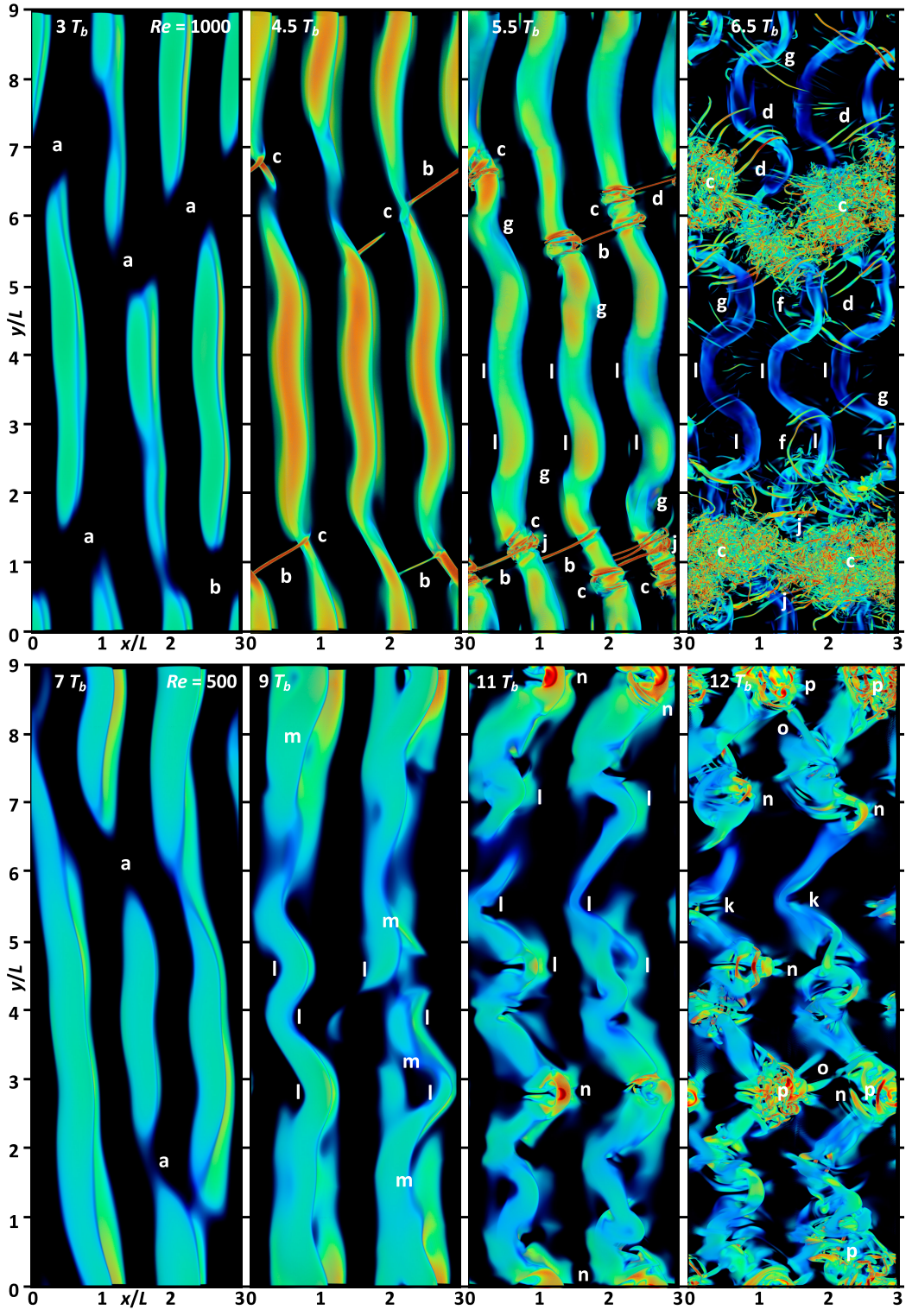

FIG. 10. As in Fig. 9, but for (top) Re = 1000 and (bottom) Re = 500. Note the later times from 3 to 6.5T_b and from 7 to 12T_b, respectively, due to the more slowly evolving KHI and T&K features in the increasingly viscous environments. See the text for details.

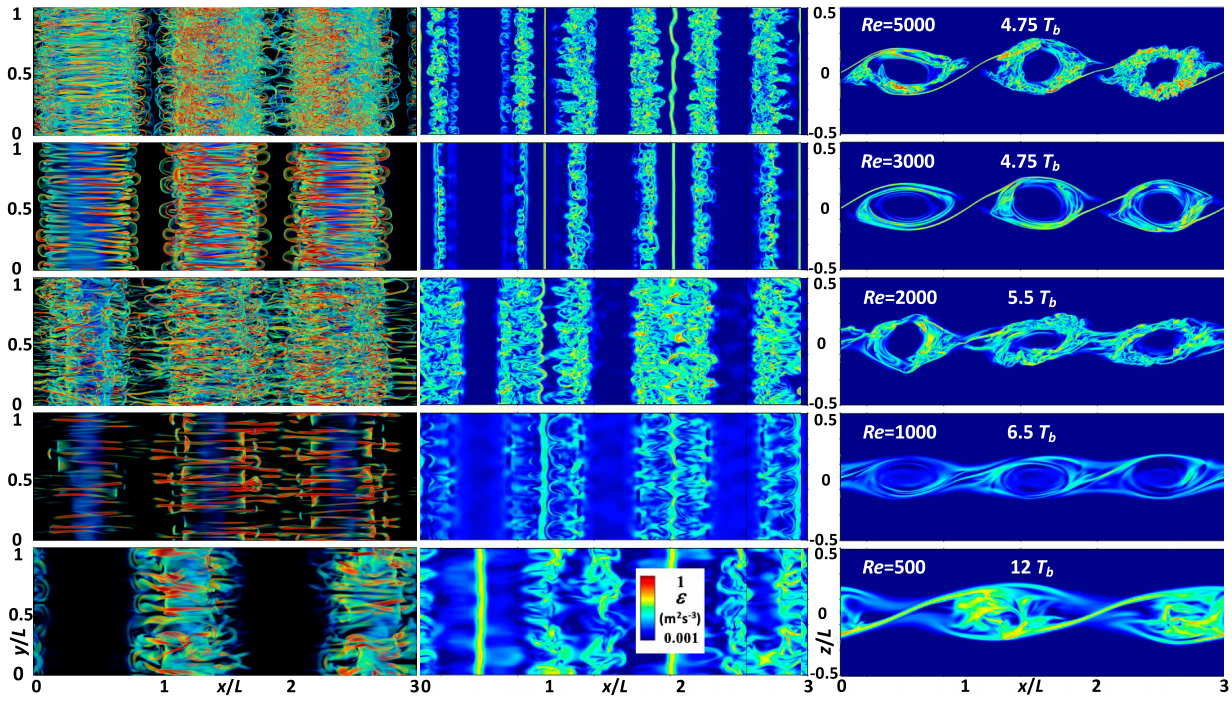

FIG. 11. As in Figs. 4–6, but for the narrow domain for Re = 5000 to 500 (from top to bottom) at the times shown at right. (left) The λ_2 viewed from above and $\log_{10}\varepsilon$ (middle) horizontal and (right) vertical cross sections at $z = 0$ and $y = 0$.

rapidly due to intense, large-scale interactions among adjacent KH billow cores at ~40%–50% of their peak magnitudes thereafter. Times at peak $\overline{\varepsilon}$ are not shown because they are after the breakdown of all coherent, initial KH billows in the wide domains.

Comparing the Re = 5000 field in Fig. 12 with the top center image in Fig. 11 reveals that secondary CIs in the wide domain are significantly less advanced at all sites where billows are even weakly influenced by T&K dynamics. They also have little or no time to arise in regions exhibiting strong initial T&K dynamics, hence contributing only very weakly to turbulence transitions and $\overline{\varepsilon}$ in this case. The same conclusions arise by examination of the corresponding fields for Re = 3000 and 2000.

As noted in the discussion of Fig. 10, T&K dynamics for Re = 1000 and 500 exhibit 1) emerging crankshaft instabilities and 2) knot formation driving larger-scale turbulence at later times. These dynamics for Re = 1000 progress rapidly from 6.5 to $7.5T_b$ (see Fig. 6 at the top and Fig. 12) due to smaller-scale vortex tubes and secondary KHI driving additional turbulence transitions. Surprisingly, they also yield the largest $\overline{\varepsilon}$ occurring ~$1T_b$ later (see Fig. 7), accompanying T&K dynamics for all Re explored here.

Evidence of the T&K dynamics accounting for the largest and narrowest $\overline{\varepsilon}$ peak for Re = 1000 at ~$8.5T_b$ is seen in $\log_{10}\varepsilon$ (x, y) at ~$7.5T_b$ in Fig. 12. The $\log_{10}\varepsilon(x, y)$ maxima at $y/L \sim$ 0–1.8 and 5–6.5 correspond closely to the strongest responses in the 3D $\lambda_2(x, y)$ field at $6.5T_b$ at the top in Fig. 10. Also seen in Fig. 12 are additional bands of enhanced $\log_{10}\varepsilon$ (x, y) centered at $y/L \sim$ 2.2, 3.3, 4.4, and 8.5, all of which correspond to $|d\phi/dy|$ maxima at the transitions between the advanced and retarded phases of the crankshaft instability along x. The implication is that T&K dynamics of these distorted billow cores initiate additional turbulence transitions due to the crankshaft instability in these regions that progress very rapidly.

Corresponding wide-domain results for Re = 500 in Fig. 12 are surprisingly very different. Here, the strong crankshaft instability, and more limited turbulence transitions in the evolving knots, results in a smaller peak $\overline{\varepsilon}$ than accompanies secondary CI in a narrow domain. This is in sharp contrast to the trend toward increasing peak and cumulative peak $\overline{\varepsilon}$ enhancements with decreasing Re for all larger Re. The cause appears to be suppression of secondary CI by the crankshaft instability in this case (compare the Re = 500 panels in Figs. 11 and 12).

We also explore the causes of peak $\overline{\varepsilon}$ in the narrow domains occurring from ~8.5 to $10T_b$. Figure 13 shows $\log_{10}\varepsilon$ (x, z) fields at $y = 0$ for Re decreasing from 5000 to 1000 at 8 and $10T_b$. They are significantly advanced relative to those shown at the right in Fig. 11, where KH billows are well defined and exhibit initial or emerging turbulence transitions. The fields in Fig. 13 reveal initial billow pairing prior to 8 T_b for Re = 2000–5000 but with decreasing efficiency for smaller Re. Pairing appears to begin for Re = 1000 by $8T_b$ but apparently does not occur thereafter. All these cases exhibit similar responses and peak $\overline{\varepsilon}$ at $10T_b$ but with that for Re = 2000 smaller by ~30% and that for Re = 2000 exhibiting much weaker $\overline{\varepsilon}$ at earlier times.

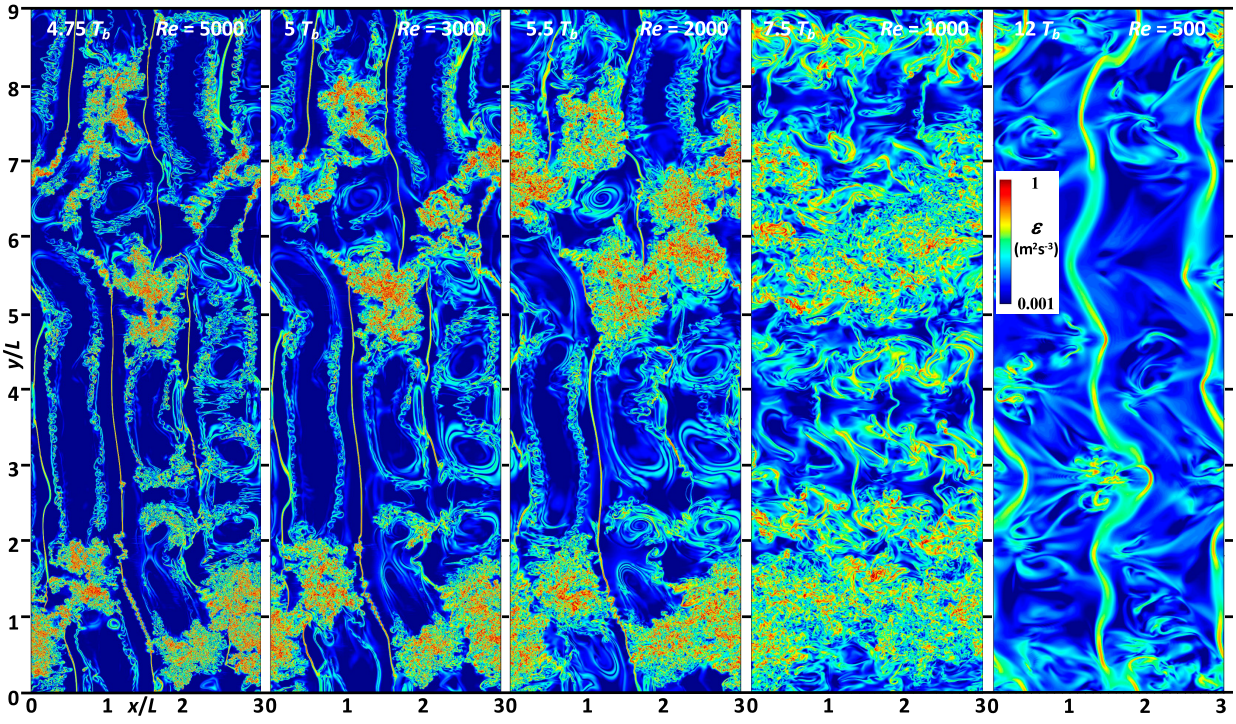

FIG. 12. Cross sections of $\log_{10}\varepsilon(x, y)$ at $z = 0$ for the wide-domain KHI T&K dynamics at Re = 5000, 3000, 2000, 1000, and 500 (from left to right) at 4.75, 5, 5.5, 7.5, and $12T_b$, respectively. Note the common ε color scale for all panels.

6. Energy dissipation rate PDFs and spectra

We now examine the evolutions of the KHI T&K responses for the five Re revealed in ε PDFs and streamwise spectra. The assessments include all data in a layer of depth $0.4L$ centered at $z = 0$ because this region contains the larger majority of KHI T&K dynamics and turbulence throughout the five evolutions.

PDFs and $\varepsilon(k)$ and $k\varepsilon(k)$ spectra are shown from left to right for decreasing Re from top to bottom in Fig. 14. Results for the five Re are shown at 1) the onset of turbulence at times of ~4, 4, 4.5, 5.5 T_b, and $11T_b$, 2) the final times shown for each case in Figs. 2, 9, and 10, and 3) extending to the peak $\overline{\varepsilon}$ seen at ~6.2, 6.5, 6.9, 8.5, and $13.4T_b$ in Fig. 7, respectively.

Influences of decreasing Re on ε magnitudes in KHI T&K dynamics

PDFs at the left in Fig. 14 reveal major differences among the various Re at the earlier and intermediate times because the large initial peaks reflect 1) the absence of initial turbulence in most regions and 2) ε magnitudes due to weak initial dynamics varying roughly as Re^{-1}. PDFs at the later times (red lines) reflect the attainment of peak turbulence intensities that vary insignificantly for the larger Re and are only ~3 times smaller for Re = 500. The long PDF tails extending to smaller $\log_{10}\varepsilon$ reveal an absence of turbulence in ~10%–15% of the central domain for Re = 1000 and larger, and a larger fraction of ~20%–30% for Re = 500, assuming a lognormal turbulence PDF in each case.

Streamwise $\varepsilon(k)$ and $k\varepsilon(k)$ "content" spectra are shown in the center and right columns in Fig. 14 with log and linear magnitude scales, respectively. Note that the spectral extent dictated by Eq. (9) to achieve true DNS decreases from ~3 decades for Re = 5000 to ~2.3 decades for Re = 500 at their peak intensities. The $\varepsilon(k)$ spectra at the first times shown (blue lines) exhibit peaks that become more prominent with decreasing Re at the primary KHI wavenumbers because those for Re = 5000 and 3000 exhibit limited streamwise wavenumber 4, whereas those for Re = 1000 and 500 exhibit only streamwise wavenumbers 3 and 2.

The $\varepsilon(k)$ spectra at the times shown have significant power at the smallest k = 1–2 k_1, for $k_1 = (2\pi/3)L$, both of which have essentially zero amplitudes at early times. Spectral slopes for Re = 2000–5000 at these times are shallow over the lowest ~2 decades of scales and consistent with those described by F22b. The $\varepsilon(k)$ "content" spectra, $k\varepsilon(k)$, shown at the right in Fig. 14 illustrate the spatial scales at which peak ε occurs for each Re (note the different amplitude scales for Re = 500). The peak $\overline{\varepsilon}$ at the final times vary roughly as Re^{-1}. Importantly, the $k\varepsilon(k)$ spectra have significantly larger amplitudes at smaller k than occur in the absence of T&K dynamics.

7. Discussion

KHI T&K dynamics were first identified in laboratory shear-flow studies by T85 and T87. Thorpe (2002) also first noted frequent evidence of these dynamics in tropospheric clouds. Subsequent observations in the atmosphere and

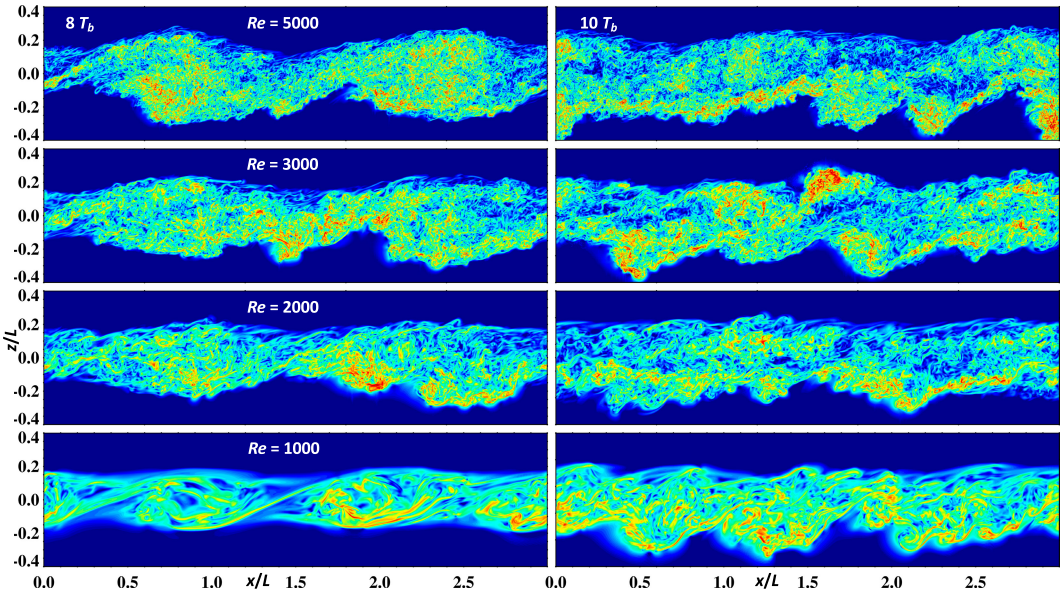

FIG. 13. As in Fig. 11, but for the narrow domain for Re = 5000 to 1000 (from top to bottom) at the times shown at right. Corresponding $\overline{\varepsilon}$ values are shown at left in Fig. 7.

oceans reviewed by F23 reveal these dynamics to be widespread, perhaps even ubiquitous, in multiscale GW environments. Of these, OH airglow and PMC imaging at high altitudes were the first to confirm T&K dynamics accompanying KH billows (H21; Kjellstrand et al. 2022).

Initial modeling in wide domains confirmed KHI dynamics to enable new and accelerated T&K pathways to turbulence and enhanced wide-domain enhanced $\overline{\varepsilon}$ maxima. F21 specified misaligned initial billows that linked to form multiple knots. F22a,b,c employed a weak initial noise seed yielding vortex tubes linking adjacent KH billows where they exhibit varying phases along their axes. A second noise seed was added in the latter studies prior to turbulence transitions to approximate the influences of pre-existing small-scale turbulence.

KHI dynamics described here were specified to enable intercomparisons of the various T&K dynamics and evolutions and their contributions to enhanced $\overline{\varepsilon}$ relative to KHI evolutions in their absence for Re varying from 5000 to 500 employing the same initial conditions. The T&K dynamics include both 1) vortex knots arising due to misaligned billow cores addressed by F21 and 2) larger and smaller vortex tubes linking adjacent KH billows addressed by F22a,b,c. An initial Ri = 0.1 enabled a maximum Re = 5000 sufficient to ensure strong secondary CI in the billow cores but no secondary KHI in the vortex sheets between billows for the specified noise seed in the absence of T&K dynamics. The same initial conditions were employed for Re of 3000, 2000, 1000, and 500 to evaluate their impacts on T&K dynamics, $\varepsilon(k)$ spectra, and peak and temporally varying $\overline{\varepsilon}$.

Results for Re = 5000 reveal that the T&K dynamics driving the earliest transitions to the most intense vortex knots are those where 2 KH billows link to 1, or 3 KH billows link to 2, either directly or via large-scale vortex tubes. Regions exhibiting multiple, smaller-scale vortex tubes emerging on vortex sheets between KH billows having large $|d\phi/dy|$ initiate secondary T&K dynamics that approach comparable local ε. Additional turbulence transitions accompany a local billow pairing event and interactions between secondary KHI and CI where they are advected into close proximity over and under the KH billows. However, these latter transitions are much less significant than the earlier, larger-scale, T&K dynamics.

These same sites drive the more rapid and intense turbulence transitions for Re = 3000 and 2000 but at successively later times due to the slower evolutions of the links among adjacent billows. Turbulence transitions for Re = 1000 and 500 are weaker and delayed due to an absence of misaligned billows and initial links via smaller-scale vortex tubes where they arise. Those for Re = 1000 occur in similar, but more confined, regions along y, than for larger Re. Those for Re = 500 exhibit no clear correlations with the transitions at larger Re, weak and widespread transitions, and slow progressions strongly constrained by viscosity. Also seen is a systematic decrease in the contributions of secondary CI to the turbulence transitions in the presence of T&K dynamics with decreasing Re relative to their occurrence in narrow domains without T&K dynamics. This suggests that secondary CI is suppressed by impacts on KH billow intensities by the increasing billow distortions due to T&K dynamics at later times.

As expected, the larger Re = 5000, 3000, and 2000 yield earlier, wide-domain $\overline{\varepsilon}$ peaks, and these arise at successively later times because the initial vortex knots (sites "c" in Figs. 2 and 10) change character somewhat and evolve more slowly for decreasing Re. Surprisingly, the largest peak $\overline{\varepsilon}$ occurs for Re = 1000. This can be traced to delayed turbulence transitions initiated by small-scale vortex tubes as the KH billows for Re = 1000 approach their largest amplitudes. The delayed transition enables peak KH billow velocity variances in wavenumbers 2 and 3 at $\sim 8.5T_b$ to be significantly larger than occur

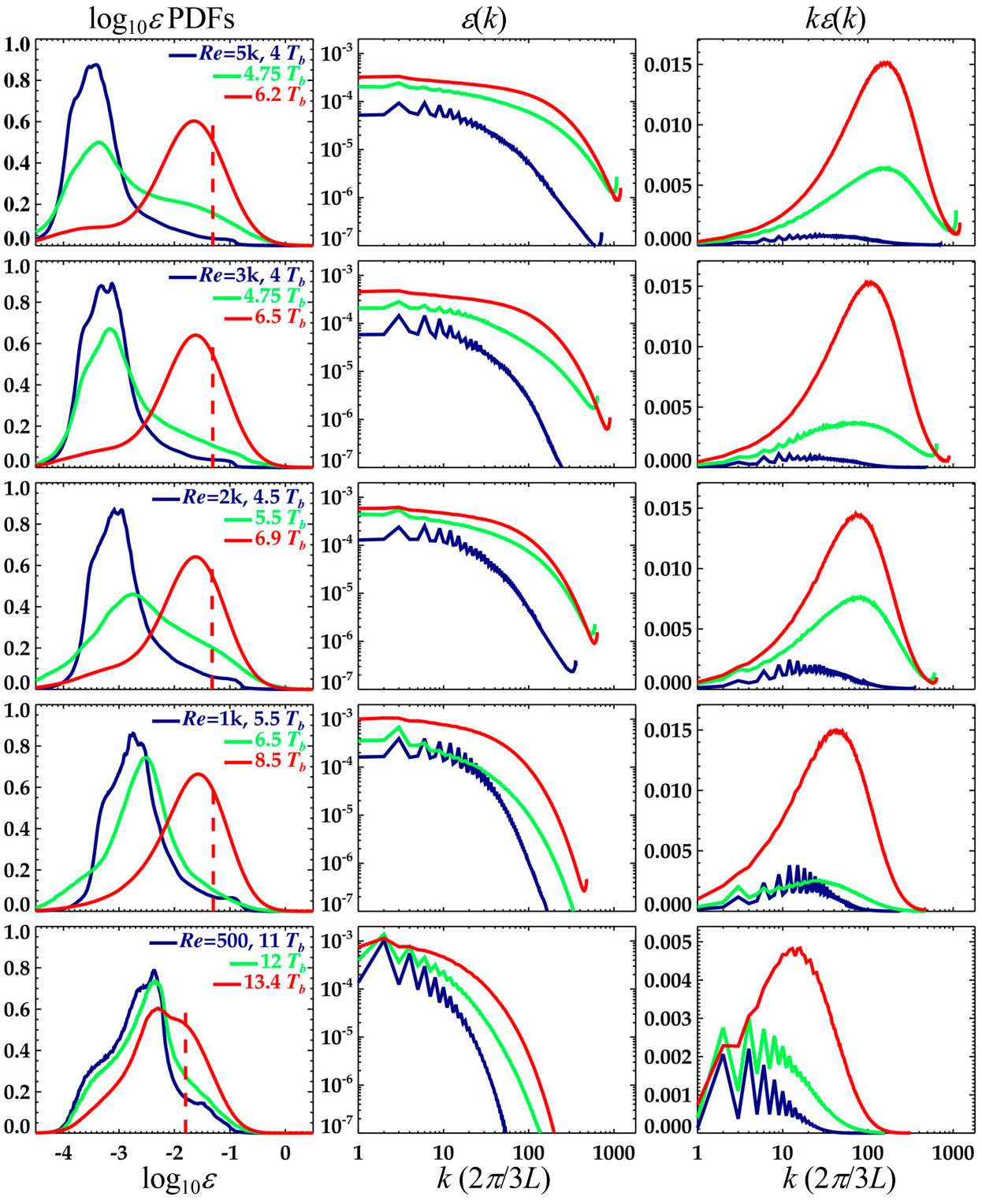

FIG. 14. (left) PDFs of $\log_{10}\varepsilon$ and streamwise spectra of (center) $\varepsilon(k)$ and (right) $k\varepsilon(k)$ assessed in wide domains for decreasing Re from top to bottom. Blue, green, and red lines show the first, second, and third times for each Re. Red dashed lines at the left show $\overline{\varepsilon}$ at the peak times. Units at center and right are MKS.

for larger Re. The result is a higher, but narrower, $\overline{\varepsilon}$ peak and a cumulative $\overline{\varepsilon}$ only ~4%–8% smaller than for the larger Re.

Peak $\overline{\varepsilon}$ for Re = 500 is ~3 times smaller and ~5–7T_b later because the larger viscosity causes significant dissipation prior to instabilities driving turbulence. Despite these differing dynamics and time scales, all the wide-domain turbulence transitions can be attributed to links between initially misaligned KH billows or via larger and smaller vortex tubes at decreasing Re. T&K dynamics cumulative $\overline{\varepsilon}$ decrease for decreasing Re. We expect enhanced turbulence intensities to yield enhanced mixing, as inferred by M23 for a KHI T&K simulation addressing mixing in the thermosphere, but that assessment will be reported elsewhere.

Temporally varying $\overline{\varepsilon}$ for the narrow-domain cases exhibits less variability for Re = 1000–5000 because they all initiate turbulence via secondary CI having roughly similar spanwise scales. Their cumulative $\overline{\varepsilon}$ decreases relative to the large y domains for decreasing Re. If these results are broadly representative of KHI events in geophysical flows, they suggest a potential for augmented mixing and transport for a significant range of geophysical parameters accompanying KHI T&K dynamics. The exception to this trend is Re = 500, which exhibits delayed temporal $\overline{\varepsilon}$ evolutions and cumulative $\overline{\varepsilon}$ peaks for both the wide and narrow domains. In this case, small-scale vortex dynamics arise at comparable times at which laminar dynamics already contributed significantly to $\overline{\varepsilon}$ in both domains.

We noted at the beginning of this section that the temporal evolution of $\overline{\varepsilon}$ described here differs from that discussed by F22b in several ways. For comparison, that in F22b is shown with red dots at 0.5 T_b intervals at the left in Fig. 7. The second noise seed in F22b is seen to significantly accelerate turbulence transitions where initial interactions between vortex tubes and billow cores arise. These drive an initial maximum $\overline{\varepsilon} \sim 0.0285\ \mathrm{m^2\ s^{-3}}$ at ~4.5T_b in the layer of depth 0.4L centered at $z = 0$ as these dynamics expand throughout the billow cores spanning these sites. A higher maximum $\overline{\varepsilon} \sim 0.038\ \mathrm{m^2\ s^{-3}}$ occurs at ~7T_b in the F22b case as the turbulence transitions expand throughout the billows at all locations and $\overline{\varepsilon}$ remains higher than seen in the Re = 5000 case described here until late times. This results in a cumulative $\overline{\varepsilon}$ that is ~2.5% larger in the F22b case at 20T_b. By comparison, the present case exhibiting knots driven by misaligned initial billows achieves a peak $\overline{\varepsilon} \sim 0.051\ \mathrm{m^2\ s^{-3}}$ that is ~35% larger, but having a full width half maximum ~35% smaller. Implications for mixing in these very different evolutions have not yet been performed.

Though not a focus of this study, our results appear to address predictions of secondary KHI and stagnation point instability (SPI) by Mashayek and Peltier (2012a,b, 2013), whose chosen Pr, Re, and Ri are the same or similar to several of our cases here and those of F21 and F22a. The most relevant cases are the narrow-domain results without T&K dynamics discussed above. However, these exhibit neither secondary KHI on the vortex sheets nor SPI for the specified profiles, parameters, and noise seed. Our wide-domain results do exhibit secondary KHI on the vortex sheets, but these are attributable to sheet deformation and intensification adjacent to regions of KH billow curvature. Secondary KHIs also arise near the stagnation points and elsewhere on the vortex sheets in both the F21 and F22a simulations, for which the initial noise seeds were significantly larger than employed in the wide-domain cases described here. In these cases, all secondary KHIs that arose on the vortex sheets between KH billows that were mis-aligned or had varying phases along y can also be attributed to T&K dynamics. Secondary CIs also arose but were significantly suppressed by billow curvature and interactions with other instability features, especially secondary KHI, but they did not compete with the stronger T&K dynamics. These results do not demonstrate that the potential secondary KHI and SPI identified by Mashayek and Peltier (2012a,b, 2013) cannot occur. However, they did not arise for the environments and initial conditions posed here.

8. Conclusions

We cannot draw broad conclusions regarding KHI T&K implications for mixing and transport based on sensitivity to Re for one Ri and a single specification of initial conditions, nor can we assert such influences without assessing them directly, as done by M23. We can, however, draw confident conclusions with respect to the parameters explored here and infer likely extensions to smaller Ri and larger Re for which there have been many previous analytic and numerical KHI studies in idealized, small domains (see, e.g., Mashayek and Peltier (2012a,b) and many previous studies).

Our results reveal that KHI T&K dynamics and enhanced $\overline{\varepsilon}$ can span a decade of Re for Ri that would enable only secondary CI in their absence without strong initial, and/or subsequent, noise seeds (i.e., F22a). If such results are found to occur for wide ranges of Re, Ri, and Pr, multiscale GW environments, and KHI T&K forms, as implied by the observations reported by F23, and the multiscale modeling described by FW23, they will likely have important implications for parameterizations of mixing and transport in the atmosphere and the oceans, given the evidence for their occurrence described by F23. Several of the results described here, and implications for likely T&K dynamics for smaller Ri and larger Re, are worth noting:

1) Our finding that KHI T&K dynamics enhance $\overline{\varepsilon}$ at constrained Re and Ri will likely also occur for smaller Ri and larger Re, suggesting widespread $\overline{\varepsilon}$ enhancements, given the range of KHI scales, environments, and Re described by F23 and FW23.
2) High-resolution atmospheric profiling reveals background turbulence to be nearly always present extending from the stable boundary layer into the MLT (Lübken et al. 2002; Strelnikov et al. 2003; Rapp et al. 2004; Balsley et al. 2006; Schneider et al. 2015); a turbulent viscosity elevated by ~1–3 decades implies a lower effective Re; however, stronger noise seeds likely favor T&K dynamics and induce competitive, potentially faster, transitions to turbulence at smaller scales (F22a).
3) Results shown here, and evidence of significant GW influences on KHI scales and their T&K dynamics demonstrated by F23 and FW23, suggest that KHI T&K dynamics arise easily as Ri decreases in intensifying multiscale GW environments; such environments are virtually always present, often emerge with decreasing Ri over short intervals,

but are neither resolved nor described adequately in regional or global models.

4) Additional instabilities of thin sheared and stratified layers, such as Holmboe and Taylor–Caulfield instabilities that arise for differing shear and stratification profiles, will likely also exhibit T&K dynamics due to environmental modulations of such layers by superpositions of various waves on multiple spatial and temporal scales.
5) Expanded explorations of the dependence of T&K dynamics on varying multiscale, and time-dependent, environments, Re, Ri, Pr, and noise seeds are required to assess their broader implications for potentially enhanced turbulence and mixing, and the parameterization of these dynamics, in geophysical fluids.

Finally, our results are specifically relevant to the "zoo" of KHI secondary instabilities described by Mashayek and Peltier (2012a,b) that arise for idealized KHI in narrow domains. Importantly, those evaluations did not enable secondary instability dynamics arising due to misaligned or varying KH billows along their axes. The apparent widespread occurrence of KHI T&K dynamics in the atmosphere and oceans described by F23 and seen to arise serendipitously in the multiscale GW DNS described by FW23 suggests that multiple new species need to be added to the zoo. Most significant are three large pachyderms: specifically vortex knots driven by 1) misaligned initial KH billows, 2) large-scale vortex tubes linking KH billows exhibiting large, local $|d\phi/dy|$, and 3) coherent "crankshaft" instabilities arising along adjacent billow cores that have major influences on smaller-scale dynamics and turbulence transitions that arise in their absence, at least at smaller Re.

Smaller, but significant, additional species include 1) multiple, smaller-scale tubes linking adjacent billows in regions of smaller $|d\phi/dy|$ that also drive intense vortex knots at slightly later times, 2) local KH billow pairing that leads to somewhat weaker knots, and 3) secondary KHI T&K dynamics that arise on the vortex sheets between adjacent KH billows and intensify strongly prior to their entrainment around the respective billows. Last, KHI T&K dynamics appear to suppress the importance of secondary CI and elevate the importance of secondary KHI in such environments extending to significantly smaller Re. Enhanced secondary KHI may then contribute to the suppression of primary KH billow pairing, as suggested by Mashayek and Peltier (2013) and seen to play a minor role in the KHI T&K results described above.

Acknowledgments. The research described here was performed under AFOSR Grant FA9550-18-1-0009 and NSF Grants AGS-2017263, AGS-2032678, AGS-2128443, and AGS-2129222 cited in GEMS. We thank the DoD HPCMP for access to significant computational resources that enabled this modeling study. We also thank three anonymous reviewers and *JAS* Editor Peter Bartello for valuable suggestions that significantly improved the paper.

Data availability statement. Our DNS modeling data reside on the DoD High Performance Computing Modernization Program systems, where all analyses and imaging were performed. These data comprise huge volumes; a single field at the peak resolution at one time is >500 GB in single precision, binary form, and these DoD systems are not open access. Hence, these data are not publicly available. The authors can provide limited such data for specific research interests.

REFERENCES

Arendt, S., D. C. Fritts, and Ø. Andreassen, 1997: The initial value problem for Kelvin vortex waves. *J. Fluid Mech.* **344**, 181–212, https://doi.org/10.1017/S0022112097005958.

Balsley, B. B., R. G. Frehlich, M. L. Jensen, and Y. Meillier, 2006: High-resolution in situ profiling through the stable boundary layer: Examination of the SBL top in terms of minimum shear, maximum stratification, and turbulence decrease. *J. Atmos. Sci.*, **63**, 1291–1307, https://doi.org/10.1175/JAS3671.1.

Blumen, W., R. Banta, S. P. Burns, D. C. Fritts, R. Newsom, G. S. Poulos, and J. Sun, 2001: Turbulence statistics of a Kelvin–Helmholtz billow event observed in the night-time boundary layer during the cooperative atmosphere–surface exchange study field program. *Dyn. Atmos. Oceans*, **34**, 189–204, https://doi.org/10.1016/S0377-0265(01)00067-7.

Fernando, H. J. S., and J. C. Weil, 2010: Whither the stable boundary layer? *Bull. Amer. Meteor. Soc.*, **91**, 1475–1484, https://doi.org/10.1175/2010BAMS2770.1.

Fritts, D. C., and L. Wang, 2023: Kelvin–Helmholtz instability "tube" and "knot" dynamics. Part II: KHI T&K dynamics in a multiscale gravity wave direct numerical simulation. *J. Atmos. Sci.*, **80**, 2439–2457, https://doi.org/10.1175/JAS-D-22-0193.1.

——, S. Arendt, and Ø. Andreassen, 1998: Vorticity dynamics in a breaking internal gravity wave. Part 2. Vortex interactions and transition to turbulence. *J. Fluid Mech.*, **367**, 47–65, https://doi.org/10.1017/S0022112098001633.

——, ——, M. A. Geller, D. A. Lawrence, J. Werne, and B. B. Balsley, 2016: Numerical modeling of multiscale dynamics at a high Reynolds Number: Instabilities, turbulence, and an assessment of Ozmidov and Thorpe scales. *J. Atmos. Sci.*, **73**, 555–578, https://doi.org/10.1175/JAS-D-14-0343.1.

——, S. A. Wieland, T. S. Lund, S. A. Thorpe, and J. H. Hecht 2021: Kelvin-Helmholtz billow interactions and instabilities in the mesosphere over the Andes Lidar Observatory: 2. Modeling and interpretation. *J. Geophys. Res. Atmos.*, **126**, e2020JD033412, https://doi.org/10.1029/2020JD033412.

——, L. Wang, T. S. Lund, and S. A. Thorpe, 2022a: Multi-scale dynamics of Kelvin–Helmholtz instabilities. Part 1. Secondary instabilities and the dynamics of tubes and knots. *J. Fluid Mech.*, **941**, A30, https://doi.org/10.1017/jfm.2021.1085.

——, ——, S. A. Thorpe, and T. S. Lund, 2022b: Multi-scale dynamics of Kelvin–Helmholtz instabilities. Part 2. Energy dissipation rates, evolutions and statistics. *J. Fluid Mech.*, **941**, A31, https://doi.org/10.1017/jfm.2021.1086.

——, ——, T. S. Lund, S. A. Thorpe, C. B. Kjellstrand, B. Kaifler, and N. Kaifler, 2022c: Multi-scale Kelvin-Helmholtz instability dynamics observed by PMC Turbo on 12 July 2018: 2. DNS modeling of KHI dynamics and PMC responses. *J. Geophys. Res. Atmos.*, **127**, e2021JD035834, https://doi.org/10.1029/2021JD035834.

——, and Coauthors, 2023: Kelvin–Helmholtz instability "tube" and "knot" dynamics. Part I: Expanding observational evidence of occurrence and environmental influences. *J. Atmos. Sci.*, **80**, 2419–2437, https://doi.org/10.1175/JAS-D-22-0189.1.

Garcia, R. R., M. López-Puertas, B. Funke, D. R. Marsh, D. E. Kinnison, A. K. Smith, and F. González-Galindo, 2014: On the distribution of CO_2 and CO in the mesosphere and lower thermosphere. *J. Geophys. Res. Atmos.*, **119**, 5700–5718, https://doi.org/10.1002/2013JD021208.

Gregg, M. C., E. A. D'Asaro, J. J. Riley, and E. Kunze, 2018: Mixing efficiency in the ocean. *Annu. Rev. Mar. Sci.*, **10**, 443–473, https://doi.org/10.1146/annurev-marine-121916-063643.

Hecht, J. H., D. C. Fritts, L. J. Gelinas, R. J. Rudy, R. L. Walterscheid, and A. Z. Liu 2021: Kelvin-Helmholtz billow interactions and instabilities in the mesosphere over the Andes Lidar observatory: 1. Observations. *J. Geophys. Res. Atmos.*, **126**, e2020JD033414, https://doi.org/10.1029/2020JD033414.

Jeong, J., and F. Hussain, 1995: On the identification of a vortex. *J. Fluid Mech.*, **285**, 69–94, https://doi.org/10.1017/S0022112095000462.

Kelvin, L., 1880: Vibrations of a columnar vortex. *Philos. Mag.*, **10**, 155–168.

Kit, E., D. Gerstenfeld, A. Y. Gelfgat, and N. V. Nikitin, 2010: Bulging and bending of Kelvin-Helmholtz billows controlled by symmetry and phase of initial perturbation. *J. Phys. Conf. Ser.*, **216**, 012019, https://doi.org/10.1088/1742-6596/216/1/012019.

Kjellstrand, C. B., and Coauthors, 2022: Multi-scale Kelvin-Helmholtz instability dynamics observed by PMC Turbo on 12 July 2018: 1. Secondary instabilities and billow interactions. *J. Geophys. Res. Atmos.*, **127**, e2021JD036232, https://doi.org/10.1029/2021JD036232.

Klaassen, G. P., and W. R. Peltier, 1985: The onset of turbulence in finite-amplitude Kelvin–Helmholtz billows. *J. Fluid Mech.*, **155**, 1–35, https://doi.org/10.1017/S0022112085001690.

——, and ——, 1991: The influence of stratification on secondary instability in free shear layers. *J. Fluid Mech.*, **227**, 71–106, https://doi.org/10.1017/S0022112091000046.

Liu, H.-L., 2019: Quantifying gravity wave forcing using the scale invariance. *Nat. Commun.*, **10**, 2605, https://doi.org/10.1038/s41467-019-10527-z.

Lübken, F.-J., M. Rapp, and P. Hoffman, 2002: Neutral air turbulence and temperatures in the vicinity of polar mesosphere summer echoes. *J. Geophys. Res.*, **107**, 4273, https://doi.org/10.1029/2001JD000915.

Luce, H., G. Hassenpflug, M. Yamamoto, M. Crochet, and S. Fukao, 2007: Range-imaging observations of cumulus convection and Kelvin-Helmholtz instabilities with the MU radar. *Radio Sci.*, **42**, RS1005, https://doi.org/10.1029/2005RS003439.

——, L. Kantha, H. Hashiguchi, D. Lawrence, T. Mix, M. Yabuki, and T. Tsuda, 2018: Vertical structure of the lower troposphere derived from MU radar, unmanned aerial vehicle, and balloon measurements during ShUREX 2015. *Prog. Earth Planet. Sci.*, **5**, 29, https://doi.org/10.1186/s40645-018-0187-4.

Mashayek, A., and W. R. Peltier, 2012a: The 'zoo' of secondary instabilities precursory to stratified shear flow transition. Part 1 Shear aligned convection, pairing, and braid instabilities. *J. Fluid Mech.*, **708**, 5–44, https://doi.org/10.1017/jfm.2012.304.

——, and ——, 2012b: The 'zoo' of secondary instabilities precursory to stratified shear flow transition. Part 2 The influence of stratification. *J. Fluid Mech.*, **708**, 45–70, https://doi.org/10.1017/jfm.2012.294.

——, and ——, 2013: Shear-induced mixing in geophysical flows: Does the route to turbulence matter to its efficiency? *J. Fluid Mech.*, **725**, 216–261, https://doi.org/10.1017/jfm.2013.176.

——, R. Ferrari, M. Nikurashin, and W. R. Peltier, 2015: Influence of enhanced abyssal diapycnal mixing on stratification and the ocean overturning circulation. *J. Phys. Oceanogr.*, **45**, 2580–2597, https://doi.org/10.1175/JPO-D-15-0039.1.

Mixa, T. S., T. S. Lund, and D. C. Fritts, 2023: Modeling Kelvin Helmholtz instability tube and knot dynamics and their impact on mixing in the lower thermosphere. *J. Geophys. Res. Atmos.*, **128**, e2023JD039249, https://doi.org/10.1029/2023JD039249.

Moin, P., and K. Mahesh, 1998: Direct numerical simulation: A tool in turbulence research. *Annu. Rev. Fluid Mech.*, **30**, 539–578, https://doi.org/10.1146/annurev.fluid.30.1.539.

Patterson, G. S., Jr., and S. A. Orszag, 1971: Spectral calculations of isotropic turbulence: Efficient removal of aliasing interactions. *Phys. Fluids*, **14**, 2538–2541, https://doi.org/10.1063/1.1693365.

Pope, S. B., 2000: *Turbulent Flows*. Vol. 1. Cambridge University Press, 771 pp.

Rapp, M., B. Strelnikov, A. Müllemann, F.-J. Lübken, and D. C. Fritts, 2004: Turbulence measurements and implications for gravity wave dissipation during the MaCWAVE/MIDAS rocket program. *Geophys. Res. Lett.*, **31**, L24S07, https://doi.org/10.1029/2003GL019325.

Rogers, M. M., and R. D. Moser, 1992: The three-dimensional evolution of a plane mixing layer: The Kelvin–Helmholtz rollup. *J. Fluid Mech.*, **243**, 183–226, https://doi.org/10.1017/S0022112092002696.

Schneider, A., M. Gerding, and F.-J. Lübken, 2015: Comparing turbulent parameters obtained from LITOS and radiosonde meas. *Atmos. Chem. Phys.*, **15**, 2159–2166, https://doi.org/10.5194/acp-15-2159-2015.

Smyth, W. D., and J. N. Moum, 2012: Ocean mixing by Kelvin-Helmholtz instability. *Oceanography*, **25** (2), 140–149, https://doi.org/10.5670/oceanog.2012.49.

Strelnikov, B., M. Rapp, and F.-J. Lübken, 2003: A new technique for the analysis of neutral air density fluctuations measured in situ in the middle atmosphere. *Geophys. Res. Lett.*, **30**, 2052, https://doi.org/10.1029/2003GL018271.

Thorpe, S. A., 1985: Laboratory observations of secondary structures in Kelvin-Helmhoitz billows and consequences for ocean mixing. *Geophys. Astrophys. Fluid Dyn.*, **34**, 175–199, https://doi.org/10.1080/03091928508245442.

——, 1987: Transitional phenomena and the development of turbulence in stratified fluids: A review. *J. Geophys. Res.*, **92**, 5231–5248, https://doi.org/10.1029/JC092iC05p05231.

——, 2002: The axial coherence of Kelvin–Helmholtz billows. *Quart. J. Roy. Meteor. Soc.*, **128**, 1529–1542, https://doi.org/10.1002/qj.200212858307.

Werne, J., and D. C. Fritts, 1999: Stratified shear turbulence: Evolution and statistics. *Geophys. Res. Lett.*, **26**, 439–442, https://doi.org/10.1029/1999GL900022.